# The Impact on Simulated Bow Echoes of Changing Grid Spacing from 3 km to 1 km in the WRF Model

DYLAN J. DODSON[a] AND WILLIAM A. GALLUS JR.[a]

[a] *Department of Geological and Atmospheric Sciences, Iowa State University, Ames, Iowa*

(Manuscript received 6 November 2023, in final form 22 February 2024, accepted 27 March 2024)

ABSTRACT: Ten bow echo events were simulated using the Weather Research and Forecasting (WRF) Model with 3- and 1-km horizontal grid spacing with both the Morrison and Thompson microphysics schemes to determine the impact of refined grid spacing on this often poorly simulated mode of convection. Simulated and observed composite reflectivities were used to classify convective mode. Skill scores were computed to quantify model performance at predicting all modes, and a new bow echo score was created to evaluate specifically the accuracy of bow echo forecasts. The full morphology score for runs using the Thompson scheme was noticeably improved by refined grid spacing, while the skill of Morrison runs did not change appreciably. However, bow echo scores for runs using both schemes improved when grid spacing was refined, with Thompson runs improving most significantly. Additionally, near storm environments were analyzed to understand why the simulated bow echoes changed as grid spacing was changed. A relationship existed between bow echo production and cold pool strength, as well as with the magnitude of microphysical cooling rates. More numerous updrafts were present in 1-km runs, leading to longer intense lines of convection which were more likely to evolve into longer-lived bow echoes in more cases. Large-scale features, such as a low-level jet orientation more perpendicular to the convective line and surface boundaries, often had to be present for bow echoes to occur in the 3-km runs.

KEYWORDS: Cold pools; Convection lines; Storm environments; Mesoscale systems; Numerical weather prediction/forecasting; Model evaluation/performance

## 1. Introduction

Mesoscale convective systems (MCSs) are responsible for a wide range of weather impacts. They are both beneficial and detrimental to those they impact, as they provide necessary rainfall for agriculture while also producing destructive weather in the form of hail, tornadoes, flooding, and wind. A bow echo is a subtype of MCS that is commonly associated with severe straight-line winds (greater than or equal to 50 kt or 25.7 m $s^{-1}$; 1 kt $\approx$ 0.51 m $s^{-1}$) and large swaths of damage as it passes through an area (Weisman 1993; Przybylinski 1995; Jirak et al. 2003; Davis et al. 2004; Wheatley et al. 2006). Bow echoes typically develop within linear MCSs, also called quasi-linear convective systems (QLCSs) but can develop from single cells as well (Klimowski et al. 2004; Wakimoto et al. 2015). Since they were first defined by Fujita (1978), they have been an important topic of research due to their destructive capabilities and threat to both life and property.

Accurate simulation of bow echoes can be difficult due to the role storm-scale processes play in their development and evolution and the need to adequately resolve these processes (Bryan and Morrison 2012; Lawson and Gallus 2016; Thielen and Gallus 2019, hereafter TG19). Some prior studies have shown that even with the use of convection-allowing models (CAMs), stratiform rain regions in MCSs are often poorly simulated (e.g., Luo et al. 2010; Snively and Gallus 2014; Morrison et al. 2015; Franklin et al. 2016; TG19) which would likely cause problems with accurate depiction of mesoscale circulations that play a role in bow echo formation. TG19 also showed that even if the stratiform rain region is simulated well, in many cases, the local accelerations that lead to bowing fail to occur.

MCSs, in general, and therefore also bow echoes, are heavily influenced by the cold pools they create, and their intensity and longevity may rely on the horizontal vorticity balance that occurs when the circulation associated with the negative buoyancy in the cold pool is of comparable magnitude but opposite sign to the horizontal vorticity in the environment ahead of them associated with low- to midlevel vertical wind shear (Rotunno et al. 1988; Weisman et al. 1988; Weisman and Rotunno 2004). Lift at the leading edge of the cold pool can trigger the development of new updrafts that sustain the system and supply hydrometeors that are advected rearward (Houze 1989). Squitieri and Gallus (2022, hereafter SG22) found that refining the horizontal grid spacing results in the development of more numerous and intense updrafts. These more abundant updrafts allowed for increased front-to-rear transport of hydrometeors, better supporting the MCS cold pool through melting and evaporative cooling.

In addition, the cold pool increases front-to-rear flow through the buoyancy differences that develop along the leading line which promote the development of a midlevel mesolow and amplification of the rear-inflow jet (RIJ; Weisman 1992; Grim et al. 2009). Damaging surface winds and pronounced bowing may be more likely when thunderstorm system downdrafts, typically driven by microphysical cooling, are able to cause a rapid descent of the RIJ (Weisman 1993). Therefore, bow echoes are sensitive to the modeling of microphysical cooling properties that influence storm-scale circulations (Adams-Selin et al. 2013; TG19).

Although studies like TG19 and SG22 suggest that it is important to use sufficiently fine grid spacings to accurately

*Corresponding author*: William A. Gallus, wgallus@iastate.edu

DOI: 10.1175/WAF-D-23-0192.1

depict convective mode, questions remain on how fine the horizontal grid spacing $\Delta x$ should be. Bryan et al. (2003) found that a $\Delta x$ as low as 100 m was required to produce a realistic representation of cloud-scale turbulence and energy transferring eddies within deep convection, while 1-km $\Delta x$ was only sufficient for resolving the larger circulations. Alternatively, some studies have found that finer $\Delta x$ does not always equate to better MCS and bow echo forecasts. An example of this was TG19, where they found that finer $\Delta x$ resulted in a higher frequency of linear systems and bow echoes, but there was no statistically significant improvement in their morphology skill score when switching from 3- to 1-km $\Delta x$. This result indicates that lines and bow echoes often occurred at the wrong times during the system evolution or with problems in depiction of stratiform rain. Similar studies have echoed the same concern when switching to a finer grid spacing (Kain et al. 2008; Schwartz et al. 2009; Snively and Gallus 2014; Weisman et al. 2023), furthering the idea that although smaller-scale processes are resolved better at finer grid spacings, this may not always equate to a more accurate forecast nor be significant enough to be worth the extra computational resources required.

The present study aims to build upon the work conducted by Snively and Gallus (2014), TG19, and SG22 but with a focus more specifically on bow echoes. This work investigates the impacts that reducing the horizontal grid spacing in the Weather Research and Forecasting (WRF) Model has on the accuracy of bow echo depiction for runs using two different microphysics schemes. It then aims to identify causes for differences seen in the depiction of bows in the 3- and 1-km simulations. Section 2 will cover the model setup, storm mode classification and scoring methodology, and calculation of cold pool variables. Section 3 presents the results of the storm mode classification and skill scores, followed by a qualitative analysis of the near-storm environment at the two grid spacings. Finally, section 4 provides a summary and discussion of these results and how they may impact bow echo forecast skill.

## 2. Data and methodology

### a. *Model configuration*

This work utilizes version 4.2.1 of the WRF Model all simulations (Powers et al. 2017; Skamarock et al. 2019). The modeling methodology replicates that used by Squitieri and Gallus (2016) and TG19. WRF simulations used the MYJ planetary boundary layer scheme (Mesinger 1993; Janjić 1994), the Dudhia shortwave scheme (Dudhia 1989), and the RRTM longwave scheme (Mlawer et al. 1997). The unified Noah land surface model (Tewari et al. 2004) was used for surface physics and the Eta similarity scheme (Monin and Obukhov 1954; Janjić 1994, 1996, 2001) for the surface layer physics. Simulations were conducted using two different microphysics schemes: the partially double-moment Thompson scheme (Thompson et al. 2008) and the fully double-moment Morrison scheme (Morrison et al. 2009). Changes in the other parameterizations listed above were found to have little impact on storm morphology in previous studies (e.g., Squitieri and Gallus 2016; TG19), and thus, no sensitivity tests were performed for those.

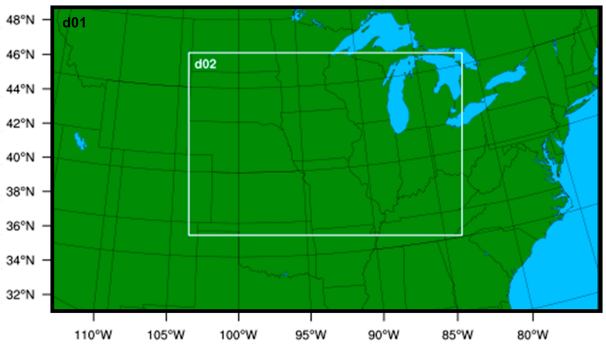


FIG. 1. An example of the one-way nested domain configuration used for the 1 Jun 2010 simulation. The inner box labeled d02 is the 1-km domain, and the larger box labeled d01 is the 3-km domain.

All simulations were initialized using the North American Mesoscale Forecast System (NAM; NOAA 2020) provided by the National Centers for Environmental Prediction (NCEP). The NAM is a regional model covering North America with a horizontal resolution of 12 km and 60 vertical levels. To test bow echo sensitivity between grid spacings $\Delta x$, the WRF simulations were run with $\Delta x$ of 3 and 1 km. This was conducted simultaneously with the 1-km domain one-way nested within the larger 3-km domain for each case. Both domains included 50 vertical levels that were assigned to specifically allow for more layers in the lowest levels of the atmosphere where processes important to MCS evolution and cold pool development take place. Vertical layers were deeper further up in the atmosphere, resulting in 25 layers above 850 hPa and 25 layers below 850 hPa (as used in Squitieri and Gallus 2016 and TG19).

The spatial and temporal settings were determined on a case-to-case basis so that the event of interest could be completely captured while also managing computational constraints. To reduce problems with lateral boundary effects, the inner (1-km) domain was configured to provide a 100-km buffer around the observed MCS of interest. That 1-km domain was then centered within a 3-km domain twice its size (Fig. 1). This resulted in a unique domain for each simulated event. All cases were initialized at 1200 UTC prior to the event, allowing roughly 6–12 h for model spinup before each event started. The model was integrated until the event of interest had either dissipated or was much weaker, usually around 24–36 h after model initialization.

While the emphasis of this study was to determine how $\Delta x$ affects bow echo depiction, sensitivity tests were performed with the microphysical schemes to allow comparisons to previous work and to supplement the present results concerning grid spacing. The Morrison microphysical scheme was chosen since prior works showed that its depiction of convective mode was less affected by changes in the horizontal grid spacing (TG19). The Thompson scheme was used since the same prior work suggested that WRF simulations saw a significant improvement in forecasting skill for convective mode when finer grid spacings were used.

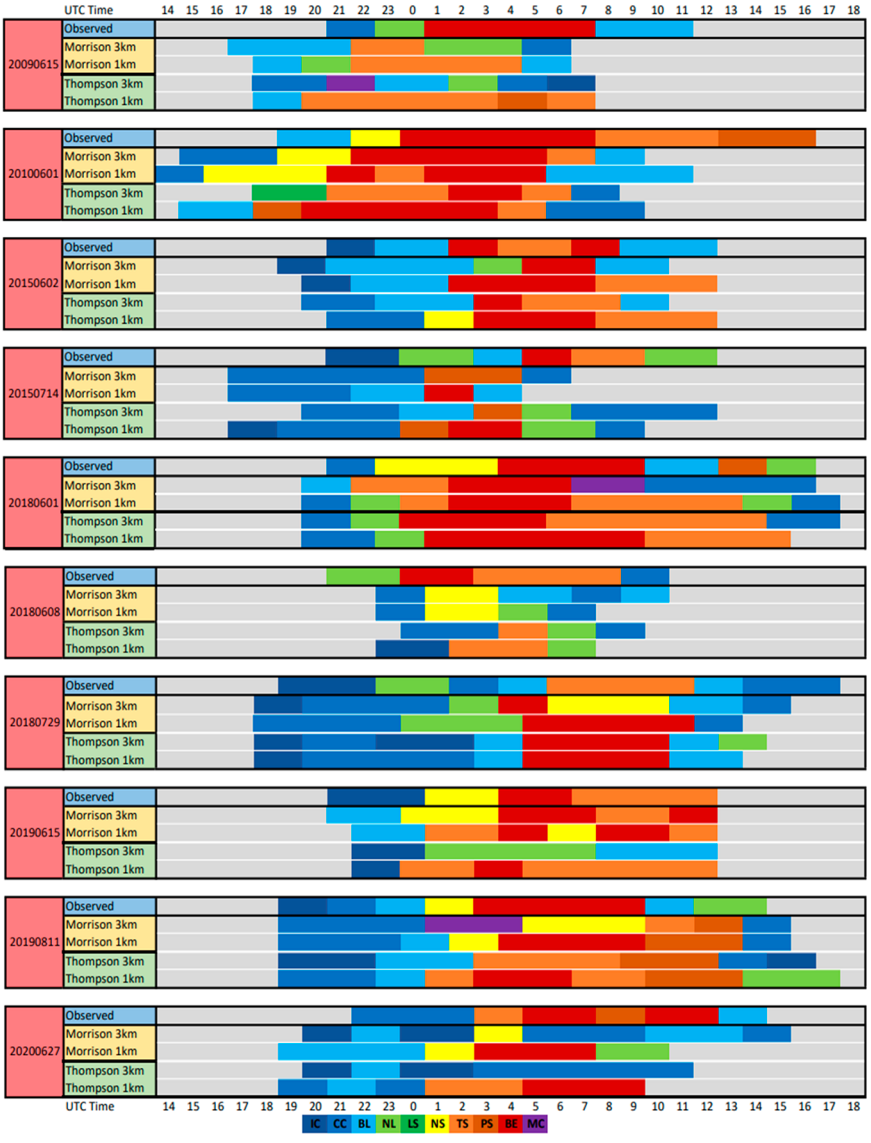


FIG. 2. Storm mode classifications for all 10 cases. Classifications are the same as those used by TG19. These modes include three cellular modes (IC, CC, and BL), five linear modes (NS, TS, PS, LS, and BE), and an NL mode. An MC mode was used to represent systems exhibiting characteristics of multiple modes. Observed morphologies are listed at the top of each case, followed by the 3- and 1-km results for the Morrison and Thompson microphysics schemes. The UTC time is listed at the top and bottom of the charts.

The case pool was comprised of a diverse set of real-world MCS events, with an emphasis on bow echo occurrence (Fig. 2). Observed and simulated bow echoes lasted from 2 to 9 h, and in some cases, multiple different periods of bowing were present during the lifetime of the system. Cases were all chosen from previous MCS morphology studies including Snively and Gallus (2014), TG19, and SG22. These studies explored the overall MCS morphology, so a subset was created for the present study using only those cases that contained either an observed bow echo or a simulated bow echo. All cases, except for 29 July 2018, contained a bow echo in the observed composite reflectivity. The 29 July 2018 case instead produced a bow echo in both the 1-km Morrison and Thompson simulations from SG22, so it was kept in the pool to provide an example of a situation where a 1-km run may inaccurately depict a bow echo that was not observed.

### *b. Storm mode classification*

To ensure a level of consistency with findings from past works, each event's storm morphology was subjectively classified using the same process used in those studies (e.g., Snively and Gallus 2014; TG19). Both the observed and simulated reflectivities for all 10 cases were classified into one of 10 different morphologies defined by Gallus et al. (2008) and

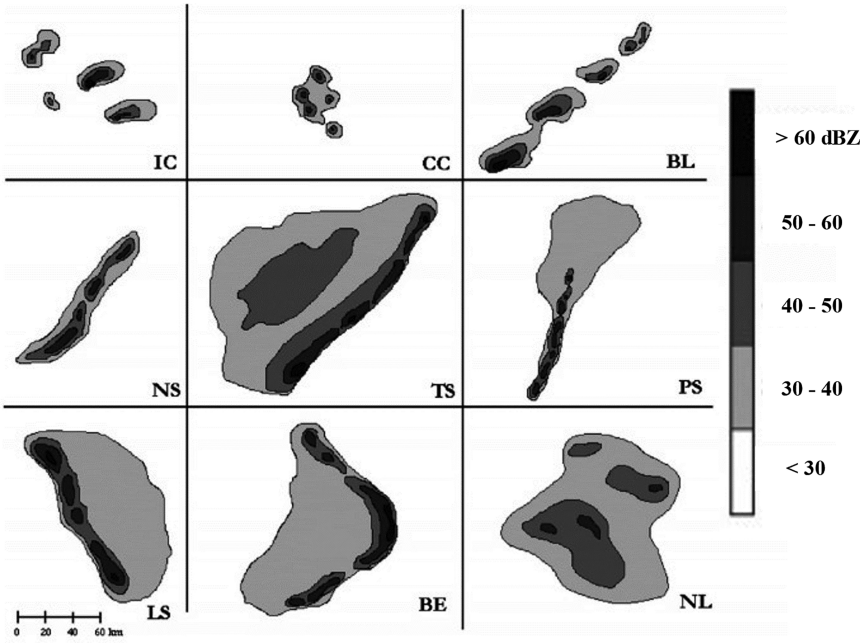


FIG. 3. The nine convective modes used for storm classification (from Gallus et al. 2008). These include the same modes defined in Fig. 2.

Snively and Gallus (2014). The observed composite reflectivity data were provided by the GridRad 3D gridded NEXRAD product (Bowman and Homeyer 2017) and the UCAR NEXRAD image archive. The 10 morphologies were spread out across four subgroups: linear, nonlinear, cellular (Fig. 3), and mixed complex (not shown), where the mixed complex (MC) classified a storm that exhibited traits from multiple morphologies. The cellular group consisted of isolated cells (ICs), clusters of cells (CCs), and broken lines (BLs). The nonlinear group contained no subtypes, and storms were simply labeled as "nonlinear" (NL). Finally, the linear storm group was divided into five classifications: no stratiform rain (NS), trailing stratiform rain (TS), parallel stratiform rain (PS), leading stratiform rain (LS), and bow echoes (BEs).

To ensure consistency when classifying storm mode, guidelines were followed that matched those used in Gallus et al. (2008), Duda and Gallus (2010), Snively and Gallus (2014), and TG19. These help to eliminate some of the subjectivity and human error that may be present when classifying storm modes. The guidelines were as follows:

1) Convective initiation was defined to occur when an area of at least 6 km × 6 km experienced a radar reflectivity greater than 40 dB$Z$. Dropping below this criterion defined the end of the storm.
2) Linear modes had to have an area of 40 dB$Z$ or greater that was at least 75 km in length with a 3:1 length-to-width ratio.
3) Stratiform regions had to have a radar reflectivity of at least 30 dB$Z$ across an area that was at least twice as wide as the convective lines to which they were attached.
4) Characteristics of a mode needed to be present for at least 2 h to be classified as that mode. If frequent hourly variations existed, the mode most representative through that timeframe was used.
5) The center of a modeled storm system had to be within 300 km of the observed system to be assumed to match the observed event and be classified. If two systems were within this region, the system in closest proximity was used.

After the storm modes were classified in both observations and simulations, the morphology skill score defined in Snively and Gallus (2014) was computed for each case. First, each system was put on a normalized time scale, where 0 represented the initiation of the system and 1 was the dissipation of the system. If a simulated system started or ended more than 3 h before or after the observed system, only the hours that fell within the 3-h buffer were used for the scoring and the others

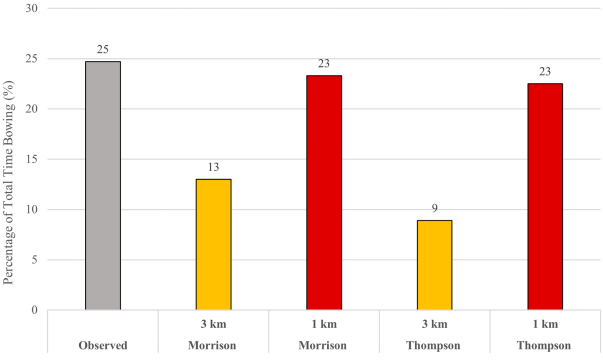


FIG. 4. The percentage of time during the system lifespan that a bow echo was present throughout all cases for both observations and the four model configurations.

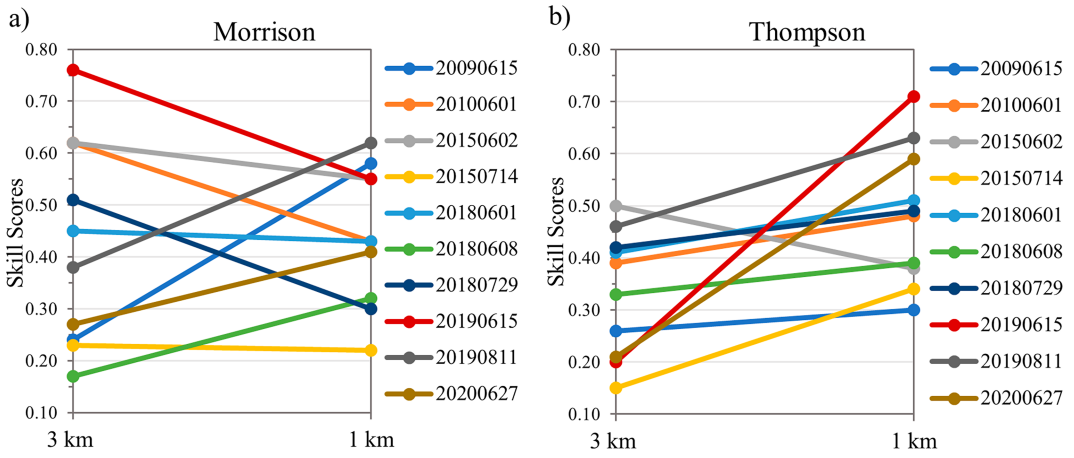


FIG. 5. Comparison of the overall morphology skill in the 3- and 1-km simulations for (a) Morrison and (b) Thompson simulations.

were not included in the normalized time scale. This time scale allowed for a comparison more focused on the morphological evolution for each respective system and provided the ability to fairly score each simulation based on how closely its evolution resembled that observed.

### c. *Skill scores*

Once the simulations were put on the normalized time scale, they were then scored based on how they compared to the observations, using the technique of Snively and Gallus (2014). The maximum score possible for each event was 1, and the lowest score possible was 0. Points were rewarded based on how similar the simulated system was to the observed, and the number of points given was dependent on the amount of normalized time that both morphologies matched (e.g., if bow echoes were both observed and simulated over the same 0.10 portion of the normalized time scale, the maximum points for that period, 0.10, would be assigned). If the exact same mode was simulated in both systems, the timeframe was awarded the maximum possible points. If the simulated system was within the same group, but the specific mode was different, it received half the possible points (e.g., both simulated linear systems, but one was trailing stratiform and the other was a bow echo). Finally, if the simulated mode was in a completely different group than the observed one (e.g., linear was simulated, but cellular was observed), it received no points for that timeframe. The points from each timeframe were then added together, creating a skill score which provided a quantitative way of comparing simulations to the observations. This was done for every simulation at 3 and 1 km for both the Morrison and Thompson runs.

A variation of this scoring system was also created to quantify the accuracy of the simulation of the bow echo alone, called the bow echo score. This scoring system utilized the same methodology as the Snively and Gallus (2014) skill score but only applied it to the period in which a bow echo was occurring in either observations or simulations. Like the Snively and Gallus (2014) skill score, a full point was awarded whenever a bow echo was simulated and observed, a half point was awarded when either the simulation or observation showed a linear mode other than a bow echo, and zero points were awarded if a linear classification was not present in both observations and the simulation. These scores allowed a quantitative comparison of bow echo depiction between runs with the two grid spacings. These scores were then also normalized based on the duration of bowing in both the observations and the simulation, which inherently introduced a penalty that accounted for over- or underforecasting of bow echoes in the simulations. This score also varied from 0 to 1.

### d. *Statistical analysis*

Once the bow echo scores were calculated for each event, hypothesis testing was used to check for statistical significance of the differences in scores from different runs. This was done using a bootstrapped paired $t$ test method. First, the original 3- and 1-km scores were subtracted from each other, resulting in an "improvement" score. Then, a population of randomized datasets was created by resampling the original dataset 10 000 times. Each time a resampled dataset was created, the values were randomly divided into a 3- and 1-km subset.


FIG. 6. Average morphology skill scores for the 3-km (yellow) and 1-km (red) Morrison and Thompson runs.

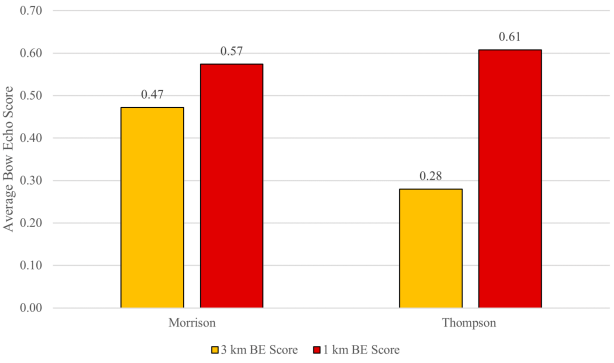


FIG. 7. Average bow echo scores for the 3-km (yellow) and 1-km (red) Morrison and Thompson simulations.

These randomized subsets of data were then compared to each other and given improvement scores, much like the observed dataset was. This was done individually for all 10 000 resampled datasets to generate a distribution of possible improvement scores. The distribution was used to conduct a one-tailed $t$ test and develop a $p$ value based on the actual difference in each case between the 1- and 3-km runs. Any resultant $p$ value outside of the 95% confidence interval was considered statistically significant.

### e. *Cold pool parameter calculations*

In addition to the morphology and scoring analyses, parameters important to the development and evolution of MCSs and bow echoes were also analyzed to understand differences between the runs with the two grid spacings. These parameters included cold pool strength, cold pool depth, and microphysical cooling rates due to the melting of graupel and ice, or the evaporation of rainwater. Potential temperature, vertical velocity, relative humidity, and wind fields were also examined to understand any differences in the near-storm environments.

Cold pool characteristics compared between 3- and 1-km runs included the negative potential temperature perturbation $\theta'$, the cold pool depth, and the cold pool parameter $C$ (m s$^{-1}$; Benjamin 1968; Rotunno et al. 1988; Weisman et al. 1988; Weisman and Rotunno 2004). The parameter $C$ is commonly used to represent the intensity of a convective cold pool and is derived from the following equation:

$$C^2 = 2\int_0^H (-B)dz, \tag{1}$$

where $H$ represents the top of the cold pool (i.e., the cold pool depth) and $B$ represents the buoyancy term derived as

$$B \equiv g\left[\frac{\theta'}{\overline{\theta}} + 0.61(q_v - \overline{q_v}) - q_c - q_r\right], \tag{2}$$

where $g$ in Eq. (2) is the acceleration due to gravity (9.81 m s$^{-2}$), $\theta'$ and $\overline{\theta}$ are the potential temperature perturbation (K) and environmental potential temperature (K), respectively, and $q_v$, $q_r$, and $q_c$ represent the mixing ratios of water vapor, rainwater, and cloud water, respectively. The term $(q_v - \overline{q_v})$ is the water vapor mixing ratio perturbation $q_v'$, the ambient water vapor mixing ratio subtracted from the total water vapor mixing ratio at each grid point.

The methods for computing $C$, $B$, $H$, and $\theta'$ replicate those in Squitieri and Gallus (2020) and Hiris and Gallus (2021). To calculate these values, the ambient environment for each time step first had to be determined. This was done by subtracting the potential temperature values at the time step 1 h ahead of the current time step, resulting in a difference in $\theta$ between the two times. These difference values were then filtered to only include positive values or areas where the environment cooled between the current time and an hour ahead. Then, the filtered potential temperature differences above the 90th percentile were used to define the location of the ambient environment out ahead of the cold pool. The 90th percentile was chosen to help delineate between any nighttime cooling and cooling due to the cold pool.

By identifying the ambient environment at each time step, the values for $\theta'$, $\overline{\theta}$, and $\overline{q_v}$ could be calculated. Prior to any calculations, $\theta'$ was first filtered so that values were only used

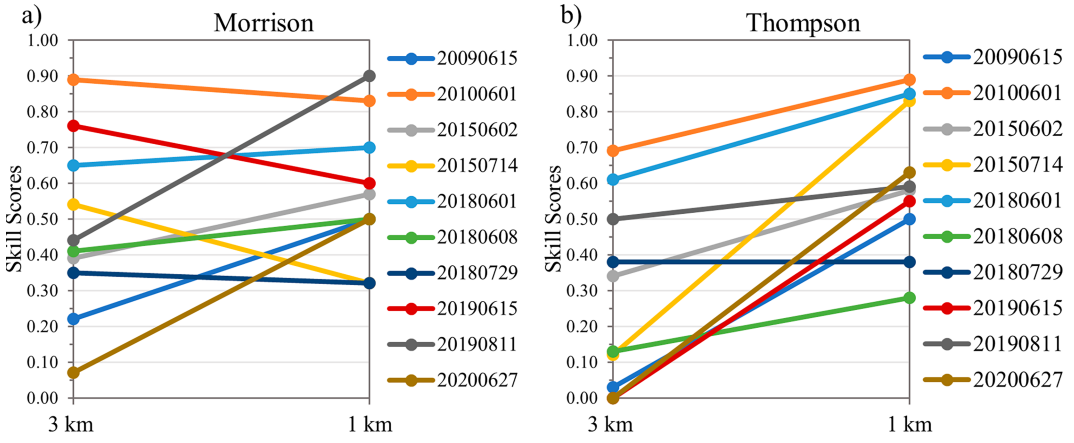


FIG. 8. Comparison of bow echo skill scores between the 3- and 1-km simulations for (a) Morrison and (b) Thompson simulations.

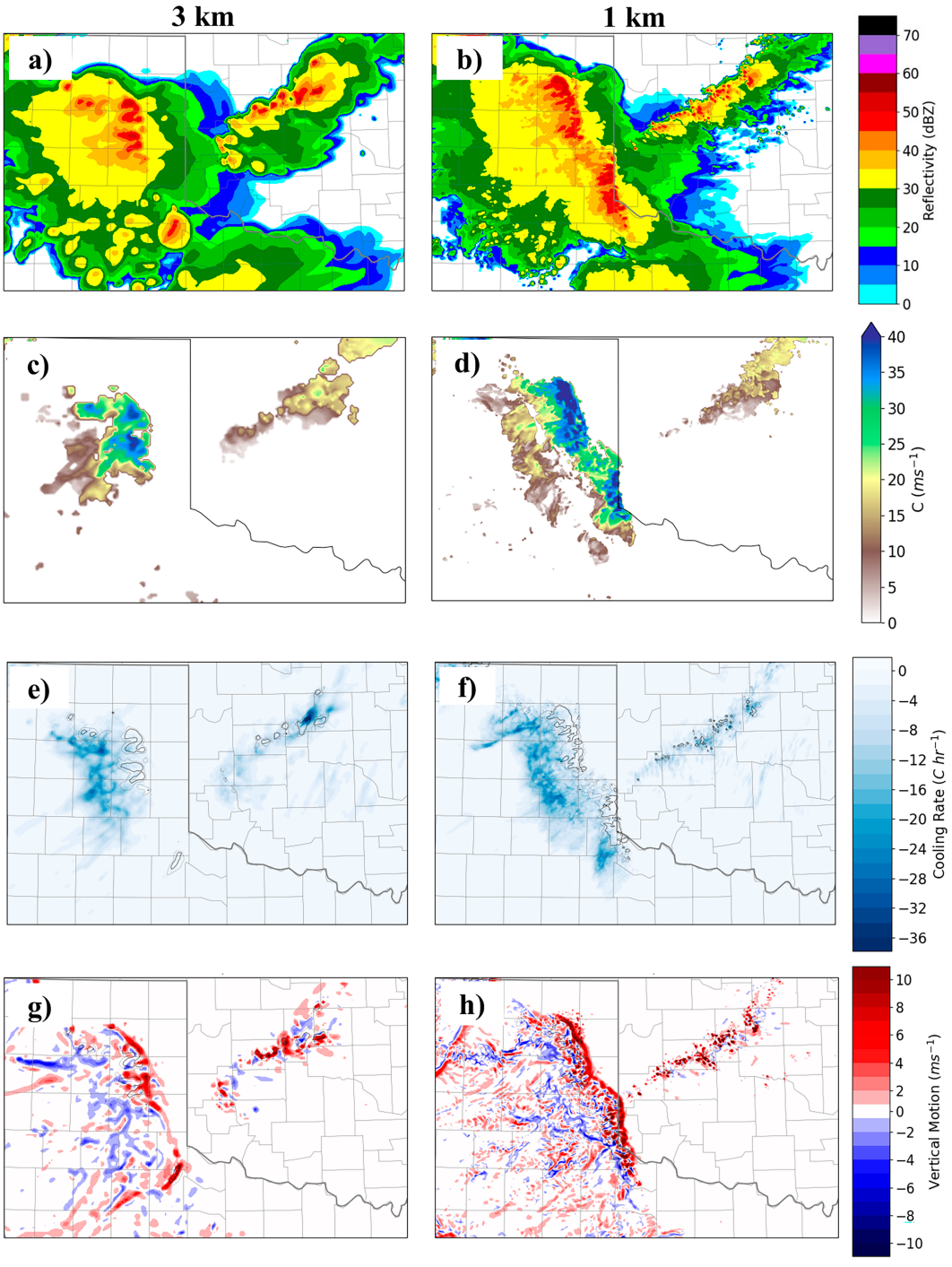


FIG. 9. The 3- and 1-km (a),(b) simulated composite reflectivity (dB$Z$), (c),(d) cold pool strength (m $s^{-1}$), (e),(f) microphysical cooling rates (from melting of snow and graupel, and evaporation of rainwater; °C $h^{-1}$), and (g),(h) 700-mb vertical velocity (m $s^{-1}$) for the 16 Jun 2019 case at 0200 UTC, 1 h before bowing occurred in the 1-km simulation. The color scale used for each plot is on the right-hand side.

if they were from points concurrent with 45 dB$Z$ or greater radar reflectivity. The cold pool depth $H$ was inferred by identifying the height at which the environment was no longer negatively buoyant (where $B \geq 0$). Finally, a Riemann sum of $B$ across all vertical layers from the surface to the top of the cold pool $H$ was used to solve Eq. (1) so that $C$ was calculated. The ambient environment and cold pool calculations were all done within smaller domains focused on the MCS of

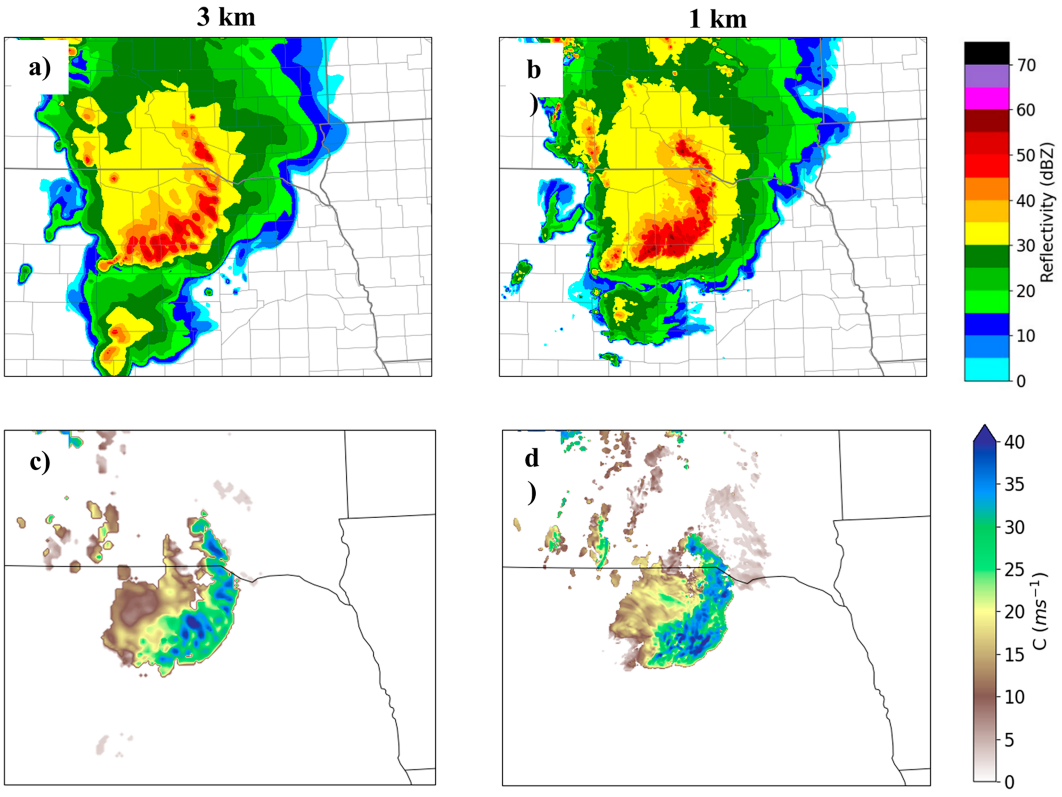


FIG. 10. The simulated composite reflectivity at (a) 3 and (b) 1 km and cold pool strength at (c) 3 and (d) 1 km for the 2 Jun 2018 case at 0100 UTC while both configurations are producing a bow echo.

interest to eliminate any contamination from other convections within the domain, as done in Hiris and Gallus (2021).

## 3. Results

### a. General case overview

An analysis of storm mode evolution was conducted for all 10 cases within the study (Fig. 2). In 8 of the 10 cases, bowing was simulated in at least one of the four configurations, while no bowing was simulated in any of the configurations for the other two cases. The 1-km Thompson and 1-km Morrison simulations produced a bow echo in all eight of these cases, but in both the 3-km Thompson and 3-km Morrison simulations, bowing occurred in only five of the cases. Of note, there were no cases where runs using either microphysics scheme produced a bow echo at 3 km without having shown one in the 1-km runs. In fact, in all cases, the duration of bowing either remained the same or increased whenever the grid spacing was refined for runs using either of the microphysics schemes.

An analysis of the fraction of the system lifetime when a convective system received a bow echo classification (Fig. 4) shows an overall increase in bow echo occurrences across the entire case pool when $\Delta x$ was switched from 3 to 1 km. This increase is more pronounced within Thompson simulations than with Morrison. These results loosely match the findings from TG19, where it was found that bow echo occurrences in the Morrison scheme only increased marginally with finer grid spacings, while runs using other microphysics schemes saw bigger increases. However, as TG19 also mentioned, an increase in bow echo occurrence as horizontal grid spacing was refined from 3 to 1 km did not imply a more accurate simulation but rather a tendency toward more bow echoes in simulations with finer grid spacing.

In the two cases where no bowing was present, runs with both microphysics schemes still produced some form of linear mode in at least the 1-km simulations. It is worth noting that signs of bowing were still present in both cases, whether that be a brief bowing segment or a rapidly accelerating line without the classic bow-like shape. However, in neither case were the features necessary for those hours to receive a bow echo classification using the guidelines in the present study produced. Although such behavior did not meet the criteria to be considered a bow echo in the present study, it is likely that operational forecasters would note these details and understand that the model may be providing enough evidence to suggest a possible bow echo.

### b. Morphology skill scores

The morphology scores for the 10 cases evidenced much run-to-run variability, especially in the 3-km Morrison simulations, where scores ranged from 0.17 to 0.76 (Fig. 5a). The 1-km Morrison scores had far less spread compared to the

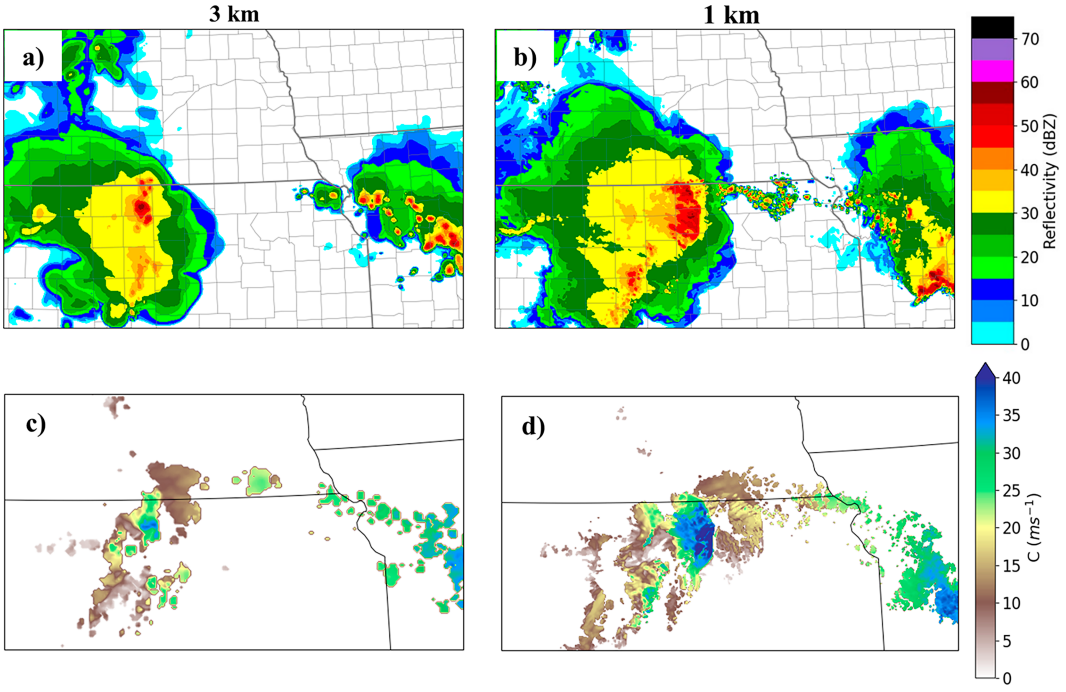


FIG. 11. The simulated composite reflectivity at (a) 3 and (b) 1 km and cold pool strength at (c) 3 and (d) 1 km for the 28 Jun 2020 case at 0500 UTC while 1 km is producing a bow echo and 3 km is not.

3-km Morrison scores. The Thompson cases, however, had less spread in scores than Morrison for the 3-km simulations, while the spread in 1-km scores stayed similar between both Morrison and Thomspon (Fig. 5b). The 3-km Morrison runs improved less than the Thompson when refining to 1-km grids, with an average improvement of only 0.02. In fact, four of the ten Morrison cases did not improve at all, although the average score for the 3-km Morrison was already much better than for the 3-km Thompson runs. On the other hand, nine of the ten Thompson simulations increased in skill when $\Delta x$ was reduced. The average improvement for all the Thompson cases was 0.15 (Fig. 6), a much greater improvement than for the Morrison scheme. In fact, the average 1-km Thompson score was slightly better than both the average 3-km Morrison and 1-km Morrison scores, and 1-km Thompson forecasts were more skillful than the 1-km Morrison forecasts for 8 out of the 10 events.

### c. *Bow echo scores*

Because the present study focuses on bow echoes, it is important to quantify improvement for the bow echo systems, and thus, an analysis was performed with the new bow echo score. Average bow echo scores improved for runs using both microphysics schemes when refining the grid spacing from 3 to 1 km (Fig. 7). However, Thompson run scores increased much more when switching to the finer $\Delta x$. The average bow echo scores for the 1-km Thompson (0.61) were higher than for the 1-km Morrison (0.57), despite the 3-km Thompson runs having a poorer 3-km score (0.28) than that for the Morrison runs (0.47). This result is consistent with TG19, which found Morrison to have the least improvement among the four microphysical schemes tested as horizontal grid spacing was refined from 3 to 1 km.

As with the overall morphology skill scores, the bow echo scores for the 3-km Morrison and 1-km Morrison varied substantially when the grid spacing was refined, again suggesting a more complex impact from refining the horizontal grid spacing in Morrison runs than in Thompson runs. However, the Morrison bow echo scores still improved with finer $\Delta x$ in six of the ten cases (Fig. 8a), which is an increase compared to the four Morrison cases whose overall morphology skill scores improved. But, despite this more consistent improvement, the difference between 1- and 3-km scores was not statistically significant while using the Morrison scheme, with a $p$ value of 0.15 from the bootstrapped hypothesis testing.

The Thompson scores (Fig. 8b) improved more consistently with all but one case (29 July 2019) improving its bow echo score when switching to the smaller $\Delta x$. In that one case, no bow echo was observed, and the periods with simulated bows only received half points for the linear modes present in the observed data, therefore resulting in no improvement in the score. The improvement in Thompson scores as grid spacing was refined was statistically significant with a $p$ value of 0.003. Therefore, there is not only an increase in bow echo occurrence when grid spacing is refined in the Thompson simulations but also an increase in bow echo forecasting skill as well.

### d. *Cold pool and microphysical cooling characteristics*

Cold pool strength values $C$ increased substantially just prior to the development of a bow echo and during its

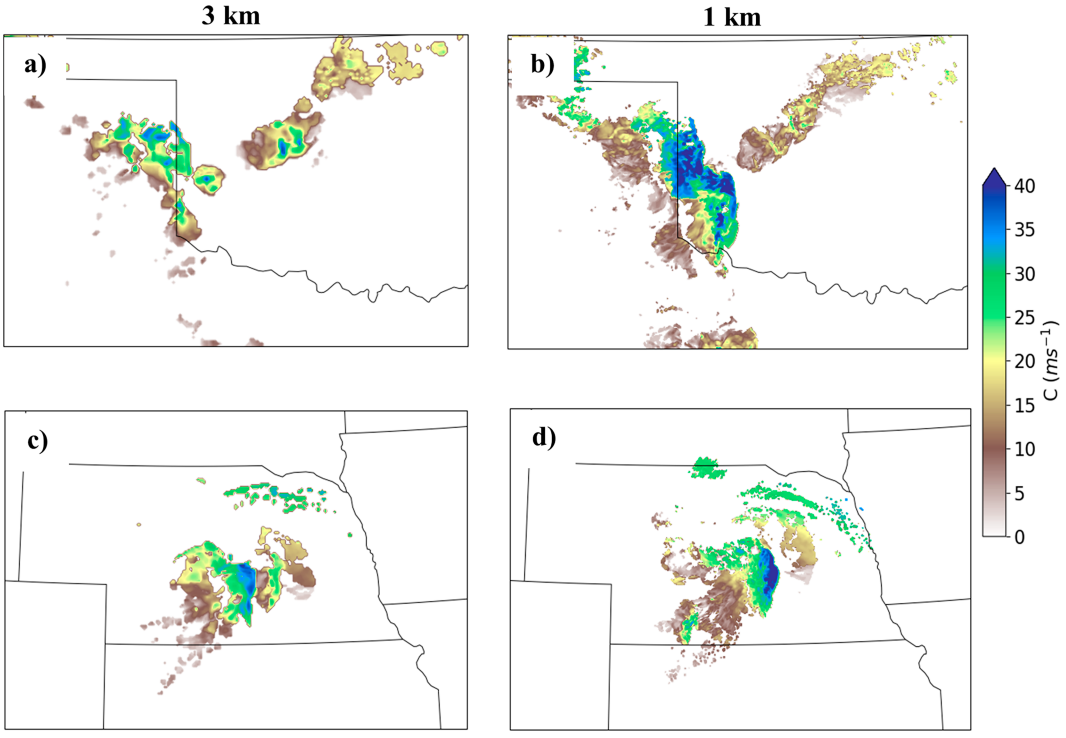


FIG. 12. The cold pool parameter for two cases where a bow echo was only produced at 1 km. (top) The 16 Jun 2019 case at 0300 UTC at (a) 3 and (b) 1 km, and (bottom) the 12 Aug 2019 case at 0600 UTC at (c) 3 and (d) 1 km. The color scale for both maps is on the right.

presence. In the four cases that a bow echo was present in both 3- and 1-km Thompson simulations, there were typically only minor differences between the 3- and 1-km simulated cold pools. The most notable of these differences was the occurrence frequently of slightly larger cold pools that often contained more expansive areas of high $C$ values (30–40 m s$^{-1}$) in the 1-km simulations (Figs. 9a–d). The 1-km simulations also showed more persistent cold pools that propagated slightly faster and generally lasted longer than the cold pools simulated at 3 km, which tended to have shorter periods where $C$ was large. However, two cases presented a similar bow echo and cold pool forecast for both the 3- and 1-km simulations (1 June and 29 July 2018). These cases both had similarly expansive cold pools with similar strong intensity in the 3- and 1-km simulations (Fig. 10). The 1-km cold pools in these two simulations were slightly more progressive in their movement, resulting in a slight displacement ahead of the 3-km cold pool at each hour. Finally, in three of the four cases where a bow echo was simulated in the 1-km run and not the 3-km run, there was a far less intense cold pool in the 3-km simulations (Figs. 11 and 12). In the other case where no 3-km bow developed, a strong cold pool did exist, but the MCS organization appeared to be hampered due to spurious convection nearby (not shown). In simulations where no bowing developed in either the 3- or 1-km simulations, the cold pools were far weaker than the runs that did produce bow echoes, often only displaying sporadic bursts of higher $C$ values. These findings further support that there is a correlation between strong cold pools and bow echo development and that 1-km simulations are more likely to produce both strong cold pools and bow echoes.

An analysis of microphysical cooling rates supports the idea that stronger cold pools are generally associated with bow echoes. Systems that produced bow echoes were often associated with enhanced cooling rates from an increase in subcloud melting of snow and graupel and evaporation of rainwater over time (Fig. 13). Both cooling processes are consistent with the deepening cold pools found for these events. Like the cold pools, regions of large cooling rates in the 1-km run were often more expansive than what was found at 3 km (Figs. 9e,f). The 1-km simulations also showed more numerous bands of large cooling rates as well (Figs. 9f and 14).

Although the 3-km cooling rates were less expansive when compared to those in the 1-km runs, there were still some areas of intense cooling, occasionally larger than the values in the 1-km runs. This is likely attributed to the difference in updraft/downdraft structures between the two grid spacings. The 1-km simulations better resolved smaller-scale circulations within the system, which resulted in more localized areas of intense values in both the cross sections (Fig. 13) and planar views (Figs. 9f and 14d). In most cases, the greatest microphysical cooling rates were associated with the strongest updrafts, which were more expansive in the 1-km simulations. However, much like the cold pool values, the 3-km simulations were still able to produce comparable cooling

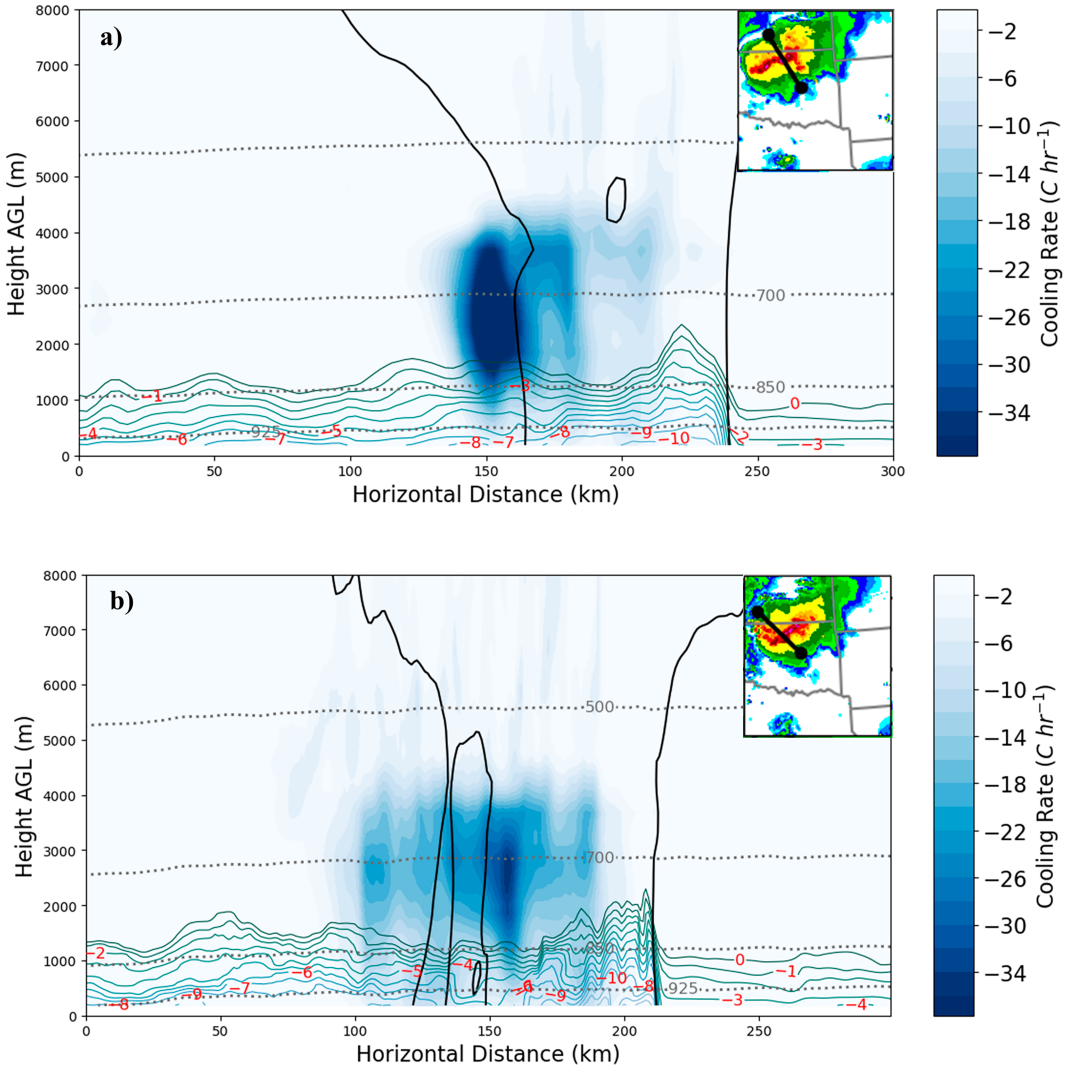


FIG. 13. Vertical cross sections of the microphysical cooling rates (as defined in Figs. 9e,f) for the 29 Jul 2018 case at (a) 0600 UTC for the 3-km simulation and (b) 0500 UTC for the 1-km simulation. Times were chosen to be most representative of the intensifying cold pool. Black lines signify the 30-dB$Z$ contour, and the light blue to green colored lines depict the cold pool structure as shown by $\theta'$. Filled contours are the cooling rates and correspond to the color bar on the right. Cross sections were taken through the eventual bowing segment of the storm and inset at the top right.

rates to the values found in the 1-km runs in a few of the cases (Fig. 14).

### e. *Resolution of vertical motion*

The resolution of vertical motion within the environment seemed to play an important role in the difference between the 3- and 1-km simulations. The 1-km runs developed more numerous updrafts in the low levels (e.g., 700 mb; 1 mb = 1 hPa) than the 3-km simulations, especially at the initial stages of the MCS when convection first began to develop (Fig. 15). This abundance of updrafts is consistent with the system in the 1-km run organizing into a convective line faster than in the 3-km run (Figs. 9g,h). It is hypothesized that the longer line of strong updrafts in the 1-km simulations led to better transport of hydrometeors rearward into the system, which resulted in more extensive latent cooling values, a stronger cold pool, and eventually a bow echo. In the 3-km simulations, upscale convective growth was still occasionally observed but with noticeably fewer updrafts present (Fig. 9g). In cases where a bow echo failed to develop at the coarser $\Delta x$, there was often a shorter and/or weaker line of updrafts than present in the 1-km runs (Figs. 9g,h). The weaker updrafts resulted in fewer hydrometeors contributing to the latent cooling processes and therefore a weaker cold pool in the 3-km runs. An increase in the updraft production from 3- to 1-km simulations may be the cause for an increase in linear systems and bow echo occurrences between the two grid spacings, as was suggested in SG22.

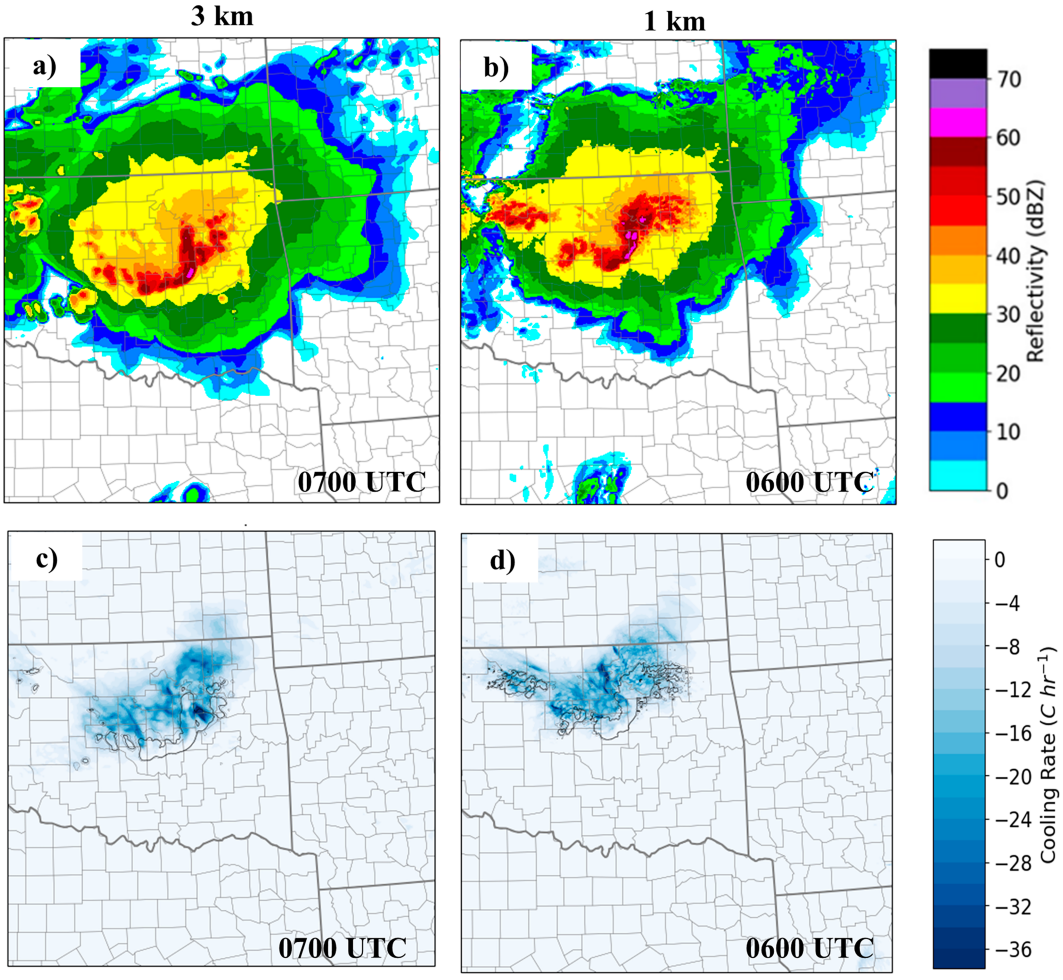


FIG. 14. The simulated (a) 3- and (b) 1-km composite reflectivities (dBZ) compared to the simulated (c) 3- and (d) 1-km cooling rates (as in Figs. 9e,f) for the 29 Jul 2018 case. Two separate times are used for 3- and 1 km due to a timing difference with each system's produced bow echo.

In cases where the bow echo depiction was similar between 3- and 1-km runs (1 June and 29 July 2018), vertical velocity fields were also quite similar. The 1-km simulations still created a longer, more intense line of convection, but the 3-km runs did not differ as much as in the cases where the 3-km runs failed to produce bowing (Fig. 16). Differences were present, with the 3-km runs struggling to keep a continuous line together for as long as the 1-km runs, likely due to the slightly

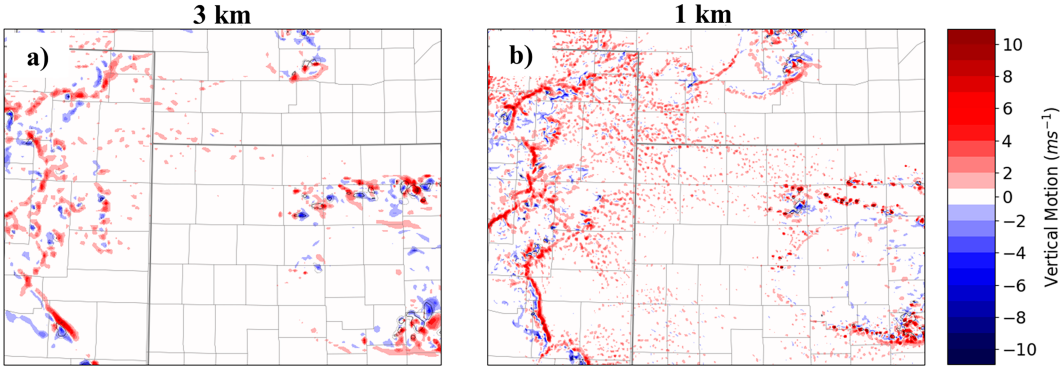


FIG. 15. Simulated 700-mb vertical velocity for 14 Jul 2015 at 2200 UTC in the early stages of convection at (a) 3- and (b) 1-km grid spacing.

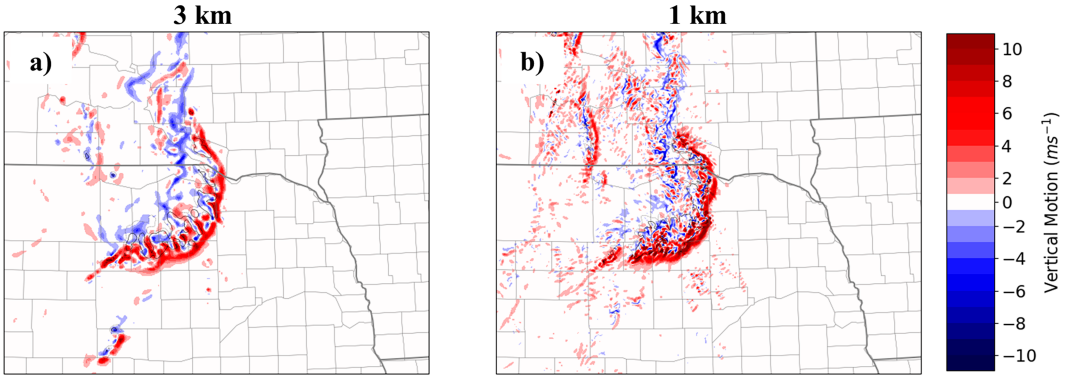


FIG. 16. Simulated 700-mb vertical velocity for 2 Jun 2018 at 0100 UTC in the early stages of convection at (a) 3- and (b) 1-km grid spacing.

weaker and less abundant updrafts within the system itself. In the 29 July 2018 case, the 3-km simulation also appeared to initially lag the 1-km line but eventually caught back up as the line of updrafts filled in. This delay resulted in a slight displacement of the 3-km system behind the 1-km one. Despite these minor differences, the 3-km lines in these two cases were still able to produce a similar bow echo evolution as their 1-km counterparts, resulting in only a small difference in bow echo scores between the two.

### *f. Larger-scale environmental features*

When the 3-km simulations were able to produce bow echoes, it was often in cases where the environment contained some larger-scale feature that helped with the evolution of the MCS. In four of the six 3-km bow echo events, a relatively strong component of low-level inflow fed directly into the observed MCSs (25 kt or more, Table 1) which was usually due to the low-level jet (LLJ) being oriented directly into the path of the systems (Fig. 17a). In the six cases where no bowing was observed in the 3-km simulations, there was a smaller line-normal component of inflow into the MCSs (16 kt or less, Table 1). In these cases, the low-level inflow was more parallel to the MCS prior to bowing (Fig. 17b).

TABLE 1. Strongest low-level (925 or 850 mb) line-normal inflow (kt) into all systems just prior to bowing. Bolded values indicate that the simulation produced a bow echo.

| | Storm inflow (kt) | |
|---|---|---|
| Case | 3 km | 1 km |
| 15 Jun 2009 | 5 | 4 |
| 1 Jun 2010 (1) | **25** | **25** |
| 1 Jun 2010 (2) | **12** | **14** |
| 1 Jun 2010 (3) | **26** | **18** |
| 2 Jun 2015 | **0** | **0** |
| 14 Jul 2015 | 16 | **15** |
| 1 Jun 2018 | **28** | **35** |
| 8 Jun 2018 | 12 | **17** |
| 29 Jul 2018 | 26 | **27** |
| 15 Jun 2019 | 0 | **2** |
| 11 Aug 2019 | 14 | **23** |
| 27 Jun 2020 | 13 | **20** |
| Avg number of BEs | 10 | 11 |
| Avg BE | **20** | **18** |

This increase in bow echo depiction in regimes of stronger line-normal flow may be due to stronger convergence along the leading edge of the developing cold pool, helping to promote stronger updrafts than what would otherwise be present in the 3-km systems. The low-level inflow also likely fed warm, unstable air into the system (figure not shown) which would help to increase the buoyancy difference along the leading edge of the cold pool. However, most notably, stronger line-normal flow often was associated with greater magnitudes of deep layer shear that could maintain a better balance with the cold pool. When comparing the 3-km cases that produced bow echoes to those that did not, higher values of 0–3- and 0–6-km bulk shear were often identified ahead of the bow echo-producing systems (not shown), further emphasizing the importance of strong line-normal flow in the 3-km simulations. It is worth noting that the differences between the 3- and 1-km wind and wind shear fields were minimal.

While the 1-km simulations likely also benefited from this stronger inflow, the higher frequency of the 1-km bow echoes in our dataset suggests that the stronger inflow was not as essential to produce bowing in those finer grid spacing runs. Two bow echoes in the 3-km dataset were able to develop despite a lack of strong line-normal low-level inflow. In both cases, a surface boundary was present orthogonal to the line of convection. Surface boundaries produce vertical vorticity, which helps in the creation of mesovortices within the MCS. These mesovortices, or bookend vortices, then enhance the RIJ resulting in a bow echo (Fig. 18). This boundary interaction became important in a few of the 1-km simulations as well. In the 27 June 2020 and 15 June 2019 cases, since the 1-km runs produced longer lines of convection, they were able to interact with the vertical vorticity along a surface boundary. The 3-km simulations for these two cases failed to produce a line far enough south to interact with the boundary at all, leading to no bow echo formation. Therefore, the 3-km simulations, in the absence of any assistance from environmental features, struggled to develop bow echoes within our case pool.

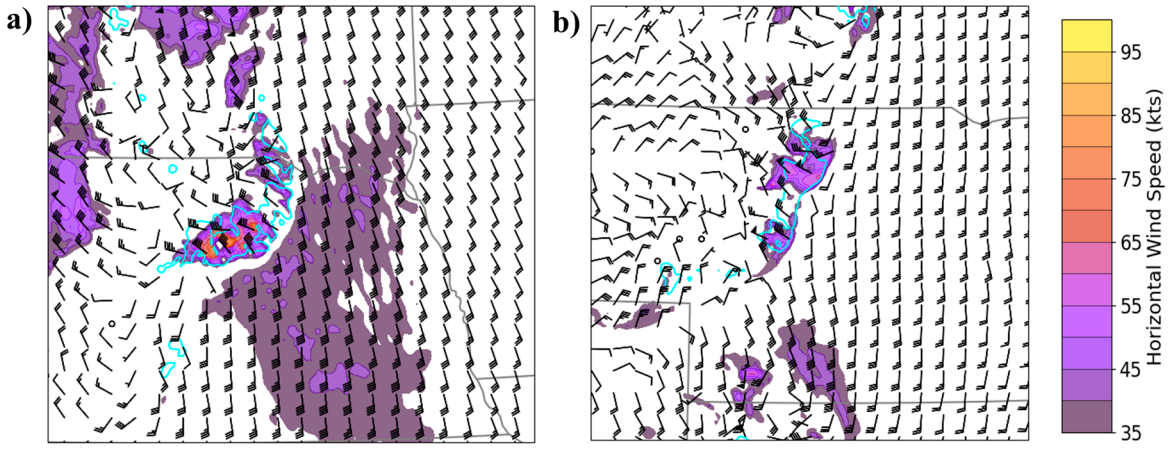


FIG. 17. The 850-mb winds from the (a) 2 Jun 2018 3-km simulation and the (b) 9 Jun 2018 3-km simulation. (a) A case where a bow echo was produced and the LLJ is providing a strong low-level inflow. (b) A situation where no bow was produced, and the environmental winds are more parallel to the system. Filled contours depict the magnitude of the 850-mb winds (kt), with the color scale featured to the right. The cyan outlines are the 40-dB$Z$ contours.

A few additional environmental parameters were examined for this study, including instability and relative humidity. Model-derived values of maximum convective available potential energy (MCAPE) showed only minor differences between the 3- and 1-km simulations, with the overall environments being virtually the same. Similarly, only small differences existed in relative humidity between the two grid spacings in the near-storm environment.

## 4. Summary and discussion

This study simulated 10 real-world MCS events and examined how bow echo depiction changed when refining the horizontal grid spacing from 3 to 1 km using both the Thompson and Morrison microphysics schemes. All simulations were given a skill score and bow echo specific skill score based on how similar the simulated reflectivity was to the observed. It was found that, within this set of cases, the refinement in grid spacing from 3 to 1 km resulted in a higher frequency of bow echoes and linear modes with both microphysics schemes, matching similar findings from TG19. The overall morphology skill scores only increased a small amount as grid spacing was refined from 3 to 1 km in the Thompson simulations, with no significant change in the Morrison simulations. However, the bow echo skill score for the Thompson simulations improved statistically significantly due to the refinement, while the Morrison score improvements were statistically insignificant. These results suggest that, although the model skill may not always improve for every convective mode, the 1-km grid spacing does result in more linear modes and bow echoes and a more accurate bow echo forecast compared to the 3-km spacing in Thompson simulations.

To develop a deeper understanding of why this improvement exists when the resolution is refined, environmental and MCS characteristics such as cold pool strength, microphysical cooling rates, vertical motion, and wind fields were investigated for the Thompson simulations. Cold pool strength played a role in the eventual development and longevity of a bow echo, with strong, persistent cold pools often present in bow echo cases, and more common in 1-km runs than in the 3-km ones. To understand why this difference was present, cooling rates were examined within the MCSs. Differences in these values were minor between 3- and 1-km simulations, with the primary difference being a noisier field at the finer

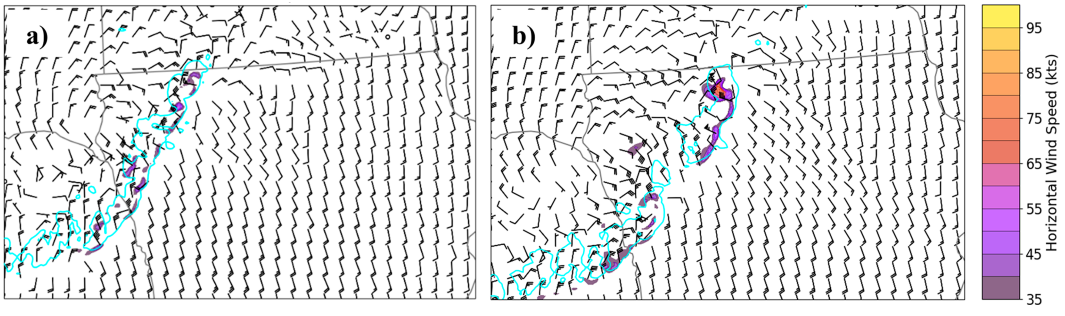


FIG. 18. The 80-m wind fields from the 2 Jun 2010 3-km simulation showing a system ingesting an outflow boundary from the north at (a) 0100 UTC. One hour later at (b) 0200 UTC, the wind barbs indicate the presence of a bookend vortex and an increase in winds on the northern edge of the storm. Filled contours depict the magnitude of the 80-m winds (kt), with the color scale featured on the right. The cyan outlines are the 40-dB$Z$ contours.

grid spacing. However, the 1-km simulations that produced bow echoes often had more expansive areas of cooling than the 3-km simulations. The noisier 1-km microphysical cooling fields were due to better-resolved vertical motion within the MCSs, which played a key factor in the development of bow echoes.

More numerous updrafts were produced in the 1-km simulations than in the 3-km simulations and associated with longer-lasting, more intense lines of updrafts. It is hypothesized that the larger and more intense line allowed for better transport of hydrometeors rearward into the system, which helped to develop stronger cold pools within the 1-km simulations. Stronger cold pools then allowed for a positive feedback by encouraging stronger updrafts (provided the cold pool remained in balance) which would transport more hydrometeors rearward within the system, further increasing the buoyancy gradient between the updraft and cold pool and ultimately resulting in a descending rear inflow jet that produced a bow echo.

Larger-scale environmental features, such as the low-level jet and surface boundaries, were important in the development of bow echoes in the 3-km simulations. It is hypothesized that strong, line-normal, low-level inflow produced by the low-level jet may provide the 3-km systems with warm, moist air that helped to intensify the cold pool. If this low-level inflow was not present, the 3-km simulations would generally not develop bow echoes unless some form of surface boundary was intercepted by the line. The boundary provided the system with the vertical vorticity necessary for the development of a mesovortex which would then intensify the RIJ in the system. It is speculated that these larger-scale features allowed the 3-km simulations to overcome issues related to less intense updrafts, making a bow echo more likely in those cases. The 1-km simulations also took advantage of these environments, especially in cases where the larger 1-km MCS was able to tap into larger-scale features that the smaller 3-km lines could not, resulting in a bow at 1 km which never occurred at 3 km.

It is important to note a few caveats to this work. First, the case pool is small, with only 10 real-world events simulated. A larger dataset would allow a better analysis of the generalizability of the results. Cases were also primarily chosen due to their production of observed bow echoes. Future work should look at more events where a bow echo was not observed to test the false alarm rate of bow echoes at different grid spacings. In addition, the subjective nature of the storm mode classifications can introduce bias. Rules established by prior works were put into place to be as consistent as possible, but human error could still be present. Finally, it is necessary to point out that the analysis of larger-scale features in the near-storm environment in the present study was mostly qualitative. Future work should examine such features quantitatively.

*Acknowledgments.* This work was supported by the National Science Foundation Grant AGS-2022888. The authors thank Brian Squitieri and Ezio Mauri for their knowledge working with and manipulating the WRF model. We thank Zach Hiris and Jon Thielen for their assistance with Python scripting and GridRad processing. Finally, thank you to Daryl Herzmann and Dave Flory for all the assistance with the Iowa State computational resources. All simulations for this project were run on the Nova supercomputer located at Iowa State University, and all postprocessing was done in Python. Finally, the author would like to point out the importance of the open source Python code which was instrumental in this study.

*Data availability statement.* The data that support the findings of this work, including the WRF model output and the data used for initial and lateral boundary conditions, are stored on Iowa State's data storage system and are available from the corresponding author upon request.

## REFERENCES

Adams-Selin, R. D., S. C. van den Heever, and R. H. Johnson, 2013: Impact of graupel parameterization schemes on idealized bow echo simulations. *Mon. Wea. Rev.*, **141**, 1241–1262, https://doi.org/10.1175/MWR-D-12-00064.1.

Benjamin, T. B., 1968: Gravity currents and related phenomena. *J. Fluid Mech.*, **31**, 209–248, https://doi.org/10.1017/S0022112068000133.

Bowman, K. P., and C. R. Homeyer, 2017: GridRad – Three-dimensional gridded NEXRAD WSR-88D radar data. Research Data Archive at the National Center for Atmospheric Research, Computational and Information Systems Laboratory, accessed 6 August 2023, https://doi.org/10.5065/D6NK3CR7.

Bryan, G. H., and H. Morrison, 2012: Sensitivity of a simulated squall line to horizontal resolution and parameterization of microphysics. *Mon. Wea. Rev.*, **140**, 202–225, https://doi.org/10.1175/MWR-D-11-00046.1.

——, J. C. Wyngaard, and J. M. Fritsch, 2003: Resolution requirements for the simulation of deep moist convection. *Mon. Wea. Rev.*, **131**, 2394–2416, https://doi.org/10.1175/1520-0493(2003)131<2394:RRFTSO>2.0.CO;2.

Davis, C., and Coauthors, 2004: The bow echo and MCV experiment: Observations and opportunities. *Bull. Amer. Meteor. Soc.*, **85**, 1075–1094, https://doi.org/10.1175/BAMS-85-8-1075.

Duda, J. D., and W. A. Gallus Jr., 2010: Spring and summer midwestern severe weather reports in supercells compared to other morphologies. *Wea. Forecasting*, **25**, 190–206, https://doi.org/10.1175/2009WAF2222338.1.

Dudhia, J., 1989: Numerical study of convection observed during the winter monsoon experiment using a mesoscale two-dimensional model. *J. Atmos. Sci.*, **46**, 3077–3107, https://doi.org/10.1175/1520-0469(1989)046<3077:NSOCOD>2.0.CO;2.

Franklin, C. N., A. Protat, D. Leroy, and E. Fontaine, 2016: Controls on phase composition and ice water content in a convection-permitting model simulation of a tropical mesoscale convective system. *Atmos. Chem. Phys.*, **16**, 8767–8789, https://doi.org/10.5194/acp-16-8767-2016.

Fujita, T. T., 1978: Manual of downburst identification for project NIMROD. SMRP Research Paper 156, 104 pp., https://hdl.handle.net/10605/261961.

Gallus, W. A., Jr., N. A. Snook, and E. V. Johnson, 2008: Spring and summer severe weather reports over the Midwest as a function of convective mode: A preliminary study. *Wea. Forecasting*, **23**, 101–113, https://doi.org/10.1175/2007WAF2006120.1.

Grim, J. A., R. M. Rauber, G. M. McFarquhar, B. F. Jewett, and D. P. Jorgensen, 2009: Development and forcing of the rear inflow jet in a rapidly developing and decaying squall line during BAMEX. *Mon. Wea. Rev.*, **137**, 1206–1229, https://doi.org/10.1175/2008MWR2503.1.

Hiris, Z. A., and W. A. Gallus Jr., 2021: On the relationship of cold pool and bulk shear magnitudes on upscale convective growth in the Great Plains of the United States. *Atmosphere*, **12**, 1019, https://doi.org/10.3390/atmos12081019.

Houze, R. A., Jr., 1989: Observed structure of mesoscale convective systems and implications for large-scale heating. *Quart. J. Roy. Meteor. Soc.*, **115**, 425–461, https://doi.org/10.1002/qj.49711548702.

Janjić, Z. I., 1994: The step-mountain eta coordinate model: Further developments of the convection, viscous sublayer, and turbulence closure schemes. *Mon. Wea. Rev.*, **122**, 927–945, https://doi.org/10.1175/1520-0493(1994)122<0927:TSMECM>2.0.CO;2.

——, 1996: The surface layer in the NCEP Eta Model. *11th Conf. on Numerical Weather Prediction*, Norfolk, VA, Amer. Meteor. Soc., Boston, MA, 354–355, https://www2.mmm.ucar.edu/wrf/users/physics/phys_refs/SURFACE_LAYER/eta_part3.pdf.

——, 2001: Nonsingular implementation of the Mellor-Yamada level 2.5 scheme in the NCEP meso model. NCEP Office Note 437, 61 pp., https://repository.library.noaa.gov/view/noaa/11409/noaa_11409_DS1.pdf.

Jirak, I. L., W. R. Cotton, and R. L. McAnelly, 2003: Satellite and radar survey of mesoscale convective system development. *Mon. Wea. Rev.*, **131**, 2428–2449, https://doi.org/10.1175/1520-0493(2003)131<2428:SARSOM>2.0.CO;2.

Kain, J. S., and Coauthors, 2008: Some practical considerations regarding horizontal resolution in the first generation of operational convection-allowing NWP. *Wea. Forecasting*, **23**, 931–952, https://doi.org/10.1175/WAF2007106.1.

Klimowski, B. A., M. R. Hjelmfelt, and M. J. Bunkers, 2004: Radar observations of the early evolution of bow echoes. *Wea. Forecasting*, **19**, 727–734, https://doi.org/10.1175/1520-0434(2004)019<0727:ROOTEE>2.0.CO;2.

Lawson, J., and W. A. Gallus Jr., 2016: On contrasting ensemble simulations of two Great Plains bow echoes. *Wea. Forecasting*, **31**, 787–810, https://doi.org/10.1175/WAF-D-15-0060.1.

Luo, Y., Y. Wang, H. Wang, Y. Zheng, and H. Morrison, 2010: Modeling convective-stratiform precipitation processes on a Mei-Yu front with the weather research and forecasting model: Comparison with observations and sensitivity to cloud microphysics parameterizations. *J. Geophys. Res.*, **115**, D18117, https://doi.org/10.1029/2010JD013873.

Mesinger, F., 1993: Forecasting upper tropospheric turbulence within the framework of the Mellor-Yamada 2.5 closure. Research activities in atmospheric and oceanic modeling, WMO/CAS/JSC WGNE Tech. Rep. 18, 4.28–4.29.

Mlawer, E. J., S. J. Taubman, P. D. Brown, M. J. Iacono, and S. A. Clough, 1997: Radiative transfer for inhomogeneous atmospheres: RRTM, a validated correlated-k model for the longwave. *J. Geophys. Res.*, **102**, 16 663–16 682, https://doi.org/10.1029/97JD00237.

Monin, A. S., and A. M. Obukhov, 1954: Basic laws of turbulent mixing in the surface layer of the atmosphere (in Russian). *Contrib. Geophys. Inst. Acad. Sci. USSR*, **151**, 163–187.

Morrison, H., G. Thompson, and V. Tatarskii, 2009: Impact of cloud microphysics on the development of trailing stratiform precipitation in a simulated squall line: Comparison of one- and two-moment schemes. *Mon. Wea. Rev.*, **137**, 991–1007, https://doi.org/10.1175/2008MWR2556.1.

——, J. A. Milbrandt, G. H. Bryan, K. Ikeda, S. A. Tessendorf, and G. Thompson, 2015: Parameterization of cloud microphysics based on the prediction of bulk ice particle properties. Part II: Case study comparisons with observations and other schemes. *J. Atmos. Sci.*, **72**, 312–339, https://doi.org/10.1175/JAS-D-14-0066.1.

NOAA, 2020: North American Mesoscale Forecast System. NCEI, accessed 3 August 2023, https://www.ncei.noaa.gov/products/weather-climate-models/north-american-mesoscale.

Powers, J. G., and Coauthors, 2017: The weather research and forecasting model: Overview, system efforts, and future directions. *Bull. Amer. Meteor. Soc.*, **98**, 1717–1737, https://doi.org/10.1175/BAMS-D-15-00308.1.

Przybylinski, R. W., 1995: The bow echo: Observations, numerical simulations, and severe weather detection methods. *Wea. Forecasting*, **10**, 203–218, https://doi.org/10.1175/1520-0434(1995)010<0203:TBEONS>2.0.CO;2.

Rotunno, R., J. B. Klemp, and M. L. Weisman, 1988: A theory for strong, long-lived squall lines. *J. Atmos. Sci.*, **45**, 463–485, https://doi.org/10.1175/1520-0469(1988)045<0463:ATFSLL>2.0.CO;2.

Schwartz, C. S., and Coauthors, 2009: Next-day convection-allowing WRF model guidance: A second look at 2-km versus 4-km grid spacing. *Mon. Wea. Rev.*, **137**, 3351–3372, https://doi.org/10.1175/2009MWR2924.1.

Skamarock, W. C., and Coauthors, 2019: A description of the Advanced Research WRF Model version 4. NCAR Tech. Note NCAR/TN-556+STR, 145 pp., https://doi.org/10.5065/1dfh-6p97.

Snively, D. V., and W. A. Gallus Jr., 2014: Prediction of convective morphology in near-cloud-permitting WRF model simulations. *Wea. Forecasting*, **29**, 130–149, https://doi.org/10.1175/WAF-D-13-00047.1.

Squitieri, B. J., and W. A. Gallus Jr., 2016: WRF forecasts of Great Plains nocturnal low-level jet-driven MCSs. Part I: Correlation between low-level jet forecast accuracy and MCS precipitation forecast skill. *Wea. Forecasting*, **31**, 1301–1323, https://doi.org/10.1175/WAF-D-15-0151.1.

——, and ——, 2020: On the forecast sensitivity of MCS cold pools and related features to horizontal grid spacing in convection-allowing WRF simulations. *Wea. Forecasting*, **35**, 325–346, https://doi.org/10.1175/WAF-D-19-0016.1.

——, and ——, 2022: On the changes in convection-allowing WRF forecasts of MCS evolution due to decreases in model horizontal and vertical grid spacing. Part I: Changes in cold pool evolution. *Wea. Forecasting*, **37**, 1903–1923, https://doi.org/10.1175/WAF-D-22-0041.1.

Tewari, M., and Coauthors, 2004: Implementation and verification of the unified NOAH land surface model in the WRF model. *20th Conf. on Weather Analysis and Forecasting/16th Conf. on Numerical Weather Prediction*, Seattle, WA, Amer. Meteor. Soc., 14.2a, https://ams.confex.com/ams/84Annual/techprogram/paper_69061.htm.

Thielen, J. E., and W. A. Gallus Jr., 2019: Influences of horizontal grid spacing and microphysics on WRF forecasts of convective morphology evolution for nocturnal MCSs in weakly forced environments. *Wea. Forecasting*, **34**, 1495–1517, https://doi.org/10.1175/WAF-D-18-0210.1.

Thompson, G., P. R. Field, R. M. Rasmussen, and W. D. Hall, 2008: Explicit forecasts of winter precipitation using an improved bulk microphysics scheme. Part II: Implementation of a new snow parameterization. *Mon. Wea. Rev.*, **136**, 5095–5115, https://doi.org/10.1175/2008MWR2387.1.

Wakimoto, R. M., P. Stauffer, and W.-C. Lee, 2015: The vertical vorticity structure within a squall line observed during BAMEX: Banded vorticity features and the evolution of a bowing segment. *Mon. Wea. Rev.*, **143**, 341–362, https://doi.org/10.1175/MWR-D-14-00246.1.

Weisman, M. L., 1992: The role of convectively generated rear-inflow jets in the evolution of long-lived mesoconvective systems. *J. Atmos. Sci.*, **49**, 1826–1847, https://doi.org/10.1175/1520-0469(1992)049<1826:TROCGR>2.0.CO;2.

——, 1993: The genesis of severe, long-lived bow echoes. *J. Atmos. Sci.*, **50**, 645–670, https://doi.org/10.1175/1520-0469(1993)050<0645:TGOSLL>2.0.CO;2.

——, and R. Rotunno, 2004: "A theory for strong long-lived squall lines" revisited. *J. Atmos. Sci.*, **61**, 361–382, https://doi.org/10.1175/1520-0469(2004)061<0361:ATFSLS>2.0.CO;2.

——, J. B. Klemp, and R. Rotunno, 1988: Structure and evolution of numerically simulated squall lines. *J. Atmos. Sci.*, **45**, 1990–2013, https://doi.org/10.1175/1520-0469(1988)045<1990:SAEONS>2.0.CO;2.

——, K. W. Manning, R. A. Sobash, and C. S. Schwartz, 2023: Simulations of severe convective systems using 1- versus 3-km grid spacing. *Wea. Forecasting*, **38**, 401–423, https://doi.org/10.1175/WAF-D-22-0112.1.

Wheatley, D. M., R. J. Trapp, and N. T. Atkins, 2006: Radar and damage analysis of severe bow echoes observed during BAMEX. *Mon. Wea. Rev.*, **134**, 791–806, https://doi.org/10.1175/MWR3100.1.